ChemElectroChem

Chemistry Europe
European Chemical Societies Publishing

Accepted Article

Title: Development of α-MnO2 Nanowire with Ni and (Ni, Co) – Cation Doping as an Efficient Bifunctional Oxygen Evolution and Oxygen Reduction Reaction Catalysts

Authors: Karuppiah Selvakumar, Velu Duraisamy, Selvaraj Venkateshwaran, Arumugam Natarajan, Almansour Abdulrahman I., Yucheng Wang, Terence Xiaoteng Liu, and Senthil Kumar Sakkarapalayam Murugesan

To be cited as: *ChemElectroChem* 10.1002/celc.202101303

Link to VoR: https://doi.org/10.1002/celc.202101303

WILEY-VCH

10.1002/celc.202101303

Development of α-MnO_2 Nanowire with Ni and (Ni, Co) – Cation Doping as an Efficient Bifunctional Oxygen Evolution and Oxygen Reduction Reaction Catalysts

Dr. Karuppiah Selvakumar [a], Mr. Velu Duraisamy [a, b], Mr. Selvaraj Venkateshwaran [a, b], Dr. Natarajan Arumugam [c], Prof. Abdulrahman I. Almansour [c], Dr. Yucheng Wang [d], Dr. Terence Xiaoteng Liu [d], and Dr. Sakkarapalayam Murugesan Senthil Kumar [*, a, b]

[a] Electroorganic and Materials Electrochemistry (EME) Division, CSIR-Central Electrochemical Research Institute (CECRI), Karaikudi-630 003, Tamil Nadu, India.

[b] Academy of Scientific and Innovative Research (AcSIR), Ghaziabad-201 002, India.

[c] Department of Chemistry, College of Science, King Saud University, P. O. Box 2455, Riyadh 11451, Saudi Arabia.

[d] Faculty of Engineering and Environment, Northumbria University, Newcastle Upon Tyne NE1 8ST, United Kingdom.

*To whom correspondence should be addressed. E-mail: smsk_2k@yahoo.com; senthilkumarsm@cecri.res.in; Phone: +91-4565-241-479.

10.1002/celc.202101303

Abstract

Manganese oxides (MnO_2) with nanowire morphology materials are a promising candidate for improving oxygen evolution and oxygen reduction reaction (OER/ORR) performance. In this work, we developed transition metal cation doping strategy into the α-MnO_2 tunnel structure to tune the Mn oxidation states and control the uniform nanowire morphology, crystalline structure in order to investigate the effect of doping over bifunctional activity. The single Ni^{2+} cation doping in α-MnO_2 with various loading concentrations resulted in 8Ni-MnO_2 exhibiting remarkable OER and ORR activity owing to their excessive concentration of Mn^{3+} and Mn^{4+} octahedral sites respectively. Further, Co^{2+} cation doping in 8Ni-MnO_2 leads to an enhanced synergistic effect that significantly improves the fraction of Mn^{3+} quantity which is confirmed by average oxidation state. For, electrochemical OER performance of 8Co-8Ni-MnO_2 exhibits a potential of 1.77 V, Tafel slope value of 68 mV dec^{-1} and lower charge transfer resistance and it is active in ORR with more positive onset potential of 0.90 V, half-wave potential of 0.80 V, better current density (4.7 mA cm^{-2}) and a four-electron pathway. Moreover, bifunctional activity ($\Delta E = E_{OER}$@10 mA cm^{-2} – ORR@$E_{1/2}$) of 8Co-8Ni-MnO_2 demonstrated 0.97 V, indicates an excellent activity in alkaline electrolyte solution.

1. Introduction

Rapid development and use of fossil fuels has resulted in increased environmental pollution and energy crises, which are significantly affected human health and daily life. Therefore, urgent need to search for a sustainable energy source to replace fossil fuels. The sustainable devices of batteries and fuel cells are directly converted to electrical energy through electrochemical reaction strategies.[1–3] Therefore, it has higher energy efficiency than fire powered plants. Oxygen electrochemistry including oxygen evolution and reduction reaction (OER/ORR) plays a vital role in batteries and fuel cells.[4–6] Due to the unsatisfactory OER/ORR reaction kinetics and slow electron transfer greatly restrict the catalytic activity and stability of fuel cell performance.[7–9] Currently, noble metal catalysts like platinum (Pt),[10,11] iridium oxide (IrO_2),[12] and ruthenium oxide (RuO_2)[13–15] are marked as an excellent catalysts toward ORR and OER. But these have many hurdles to pragmatic activities including scarcity, high cost, low durability and stability.[16,17] Hence, these are bottlenecks which renders low catalytic activity and poor performance. Thus, an urgent need for electrocatalysts which would improve the bifunctional performance of regenerative fuel cells. Till now, finding out low cost, highly active and durable catalysts are a big challenge in this research field.

To address these issues, various alternative catalysts have been studied for improving OER/ORR activity such as transition metals, metal oxides,[18–20] sulfides[21] and carbides.[22] Among the various catalysts reported to date, manganese oxide (MnO_2) is regarded as a cost-effective, outstanding bifunctional catalyst in fuel cells.[23,24] MnO_2 not only easily adsorb the H and OH species but it also supressess the peroxide production, resulting in improved ORR kinetics.[23] In particular, Mn is mostly available in the form of [MnO_6] octahedral sites in +2 and

+3 states. The Mn^{3+} in octahedral sites posses one electron occupancy in e_g orbital thereby increasing the oxygen adsorption which improves ORR activity.[25]

In addition, MnOx occurs in different kinds of stoichiometric forms, crystallographic phases, and geometric shapes (α, β, and δ-types), which are greatly alter their catalytic performance and stability.[26] Remarkably, MnO_2 has a various types of tunnel structures, such as the α-MnO_2 crystal lattice which is composed of [2 × 2] and [1 × 1] tunnel structures and tunnel size is 4.6 Å. The β-MnO_2 consists of [1 × 1] type tunnel structures and the tunnel size is 2.3 Å. The γ-MnO_2 composed of both tunnel structures [1 × 1] and [2 × 2] with a size of 0.7 Å. The variation of tunnel structures effectively enhances the OER activity.[27,28]

Especially, α-MnO_2 demonstrates the hollandite-type MnO_2, which is highly active in OER. In particular, 1D nanowire of α-MnO_2 demonstrate excellent catalytic activity compare with nanoflower, nanorod, nanosheets and platelets.[29,30] In addition, α-MnO_2 (I4/m) composes the edges of the MnO_6 octahedral tunnels easily stabilizing the ions and water molecules thereby improving Mn^{3+} and catalytic sites.[31] Further, creating oxygen vacancies in the α-MnO_2 structure is an additional way to increase the catalytic activity. The oxygen vacancies effectively tune the active sites, electronic and geometric structures along with chemical properties. Recently, our group reported the silica template-derived MnO_2 exhibits better bifunctional activity owing to their promotion of oxygen vacancy site and pore arrangement.[32] Similarly, in another report by Cheng *et al*.[33] the existence of oxygen vacancies enriches the interaction between MnO_2 and oxygen-containing species, which favours the catalytic activity. However, the OER/ORR activity of an α-MnO_2 is far more sluggish than that of benchmark catalysts (Pt, IrO_2 and RuO_2) owing to their poor conductivity, limited oxygen vacancy sites and variations in morphology.

Further, doping of metal atoms with α-MnO_2 is an efficient strategy for tailoring the oxygen defects, surface sites, valence of Mn and electron transfer ability. Lee *et al*.,[34] suggested that the Fe substitution in α-MnO_2 causes significant enhancement in the structural order of MnO_6 octahedral which showed remarkable charge transfer performance. Single/co-doping of metal ions, especially Ni, and Co into α-MnO_2 matrix has proven one of the excellent ways to improve the bifunctional activity towards OER and ORR. The Ni possess favourable interaction with OH species and follows the Sabatier principle for material design attributes the remarkable OER activity than Fe and Mn-based materials.[35] In an another attempt, amorphous birnessite MnOx-deposited on carbon as a composite doped with Ni/Mg cations are found to lead to higher n-values, providing an evidence for the improved ORR mechanism toward a direct four-electron mechanism.[36] They found that the Ni-doped catalyst leads to a significantly low amount of peroxide intermediate formation due to the fact that the Ni-doped material paved a way to stabilize the Mn^{3+} active site produced during ORR. Similarly, the activity of the spinel-type Mn_3O_4 catalysts has also been enhanced significantly during the addition of metal ion dopants ($Cu_xMn_3{-}xO_4$) in their lattices.[37]

Lambert *et al*.[38] recently prepared Ni and Cu-doped α-MnO_2 nanowire materials and found that their activity was significantly higher when compared to the bare α-MnO_2 nanowire even though the doped materials possess low BET surface area. They explained that such observed higher current density observed for both Ni- and Cu-doped materials were due to improved electron-transfer kinetics during ORR. They also found that simple physical blending with a graphene-like carbon the 20% Cu-α-MnO_2 catalyst displayed ORR activity which is very close to that of the benchmark 20% Pt/C catalyst. However, it is difficult to pinpoint exactly the influence of Cu ions on the activity of Cu-α-MnO_2 for the ORR. Furthermore, cobalt-doped

MnO_2 nanosheet with more oxygen vacancies are accountable for OER activity reported by Zhao *et al*.[39] In general, cation doping of MnO_2 has previously been suggested to revise the Mn^{3+} quantity which in turn enhances the electrocatalytic activity.[40,41] However, it is worth to point that dual cation doping in MnO_2 significantly damages the morphology and octahedral sites which led to a dramatic decrease in surface area and the electrochemical performance. Based on the above fact it is very crucial to establish a dual bi-valent cation doping process without affecting crystallography, morphology, surface area and the catalytic activity.

To solve these problems, we intended to alter the electronic properties and control the α-MnO_2 nanowire morphology by incorporating similar size single bivalent (Ni^{2+}) and dual bivalent cations (Ni^{2+}, Co^{2+}) into their channels. Initially, we optimized the Ni^{2+} cation loading by preparing various amounts of Ni^{2+} incorporated α-MnO_2 nanowire morphology by hydrothermal process (**Figure 1a**). Then the resultant Ni^{2+}-doped-α-MnO_2 nanowire materials exhibit better activity towards OER/ORR in 0.1 M KOH solution. The best Ni^{2+}-doped-α-MnO_2 material has been selected for dual doping of Co^{2+} using a similar hydrothermal procedure. The influence of Ni^{2+} percentage on the MnO_2 tunnel structure and electrochemical behaviour of the synthesised Ni^{2+}-doped-α-MnO_2 nanowire materials were systematically studied. Moreover, the electrochemical OER/ORR analysis of the 8Co-8Ni-MnO_2 catalyst demonstrates superior bifunctional activity owing to their high density of Mn^{3+} and Mn^{4+} sites.

2. Result and Discussions

2.1 Doping of nickel ion into α-MnO_2 Nanowires

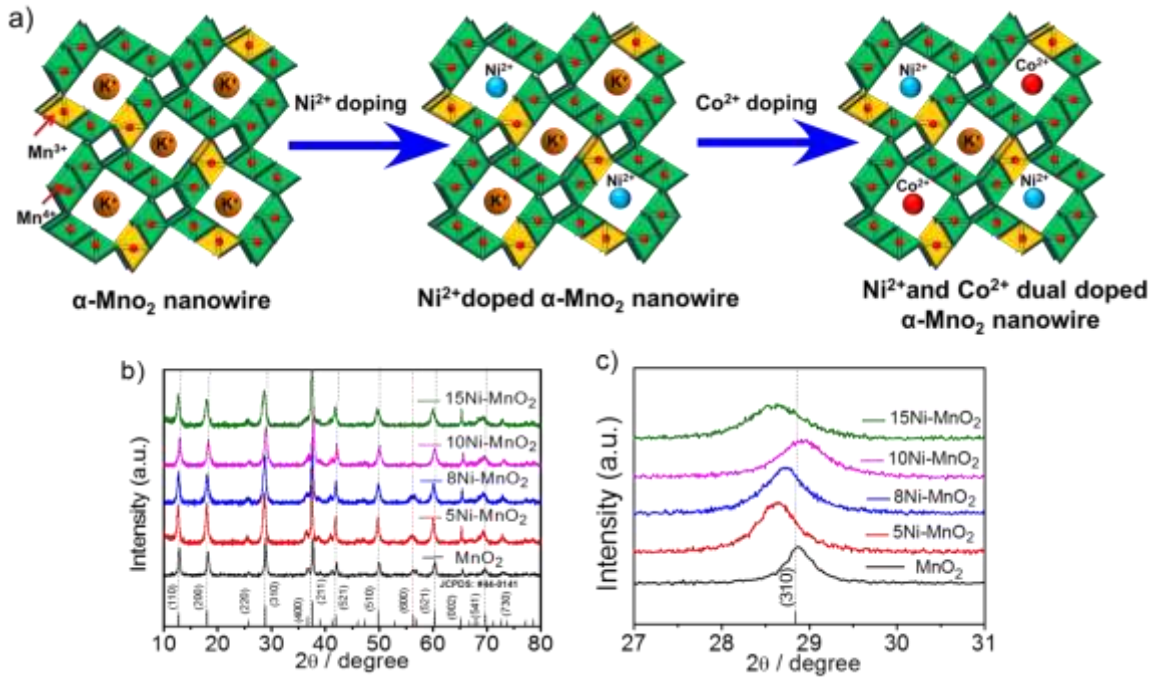

Figure 1. Schematic view of synthesis of the Ni and Co dual doped α-MnO_2 materials by hydrothermal approach. (b) XRD patterns of four different Ni-doped MnO_2 nanowire materials. (c) High magnified view of (310) plane shows peak shift and peak broadening in XRD patterns of 5Ni-MnO_2, 8Ni-MnO_2, 10Ni-MnO_2 and 15Ni-MnO_2 materials.

The XRD patterns of various Ni-doped MnO_2 nanowires are given in **Figure 1b**. The observed 2θ diffraction peaks are in good agreement with JCPDS pattern no 44-0141 of body-centered tetragonal MnO_2 material and the space group of 14/m, a=b= 9.784 A°, c= 2.863 A°. [29,30] The absence of additional peaks indicates the nickel ions are successfully doped into the crystal lattice of MnO_2 as cations by replacing potassium ions which are composed of MnO_6 octahedra structure with [2 × 2] tunnels.[42] Comparison of undoped MnO_2 material, the variations in intensity, peak broadening and peak shift was exhibited in the Ni-doped MnO_2 nanowire (**Figure 1c**) revealed differences in the crystal domain size. This could be the result of

10.1002/celc.202101303

insertion of nickel into the MnO_2 lattice without affecting the crystal structure of Mn octahedral and alters the electronic property of the α-MnO_2 material.

In addition to that, we also noticed the disappearance of (600) plane for high dopant samples such as 10Ni-MnO_2 and 15Ni-MnO_2. We have measured the full width half maximum (FWHM) value for the (310) plane and calculated d-spacing value and crystallite size (using scherrer equation) were given in **Table S1**. The values conclude that increasing the nickel dopant from 5 mmol to 15 mmol reduces the crystallite size of the α-MnO_2 nanowire materials.

Figure S1a shows the FTIR spectra and it contains the vibrations at 466 cm^{-1}, 520 cm^{-1} and 716 cm^{-1} that are attributed to the stretching vibrations of M-O bond (M = metal) which confirm the formation of α-MnO_2 frameworks. In Raman spectra (**Figure S1b**), three diagnostic bands were observed. The band at low-frequency region of 180 cm^{-1} and high-frequency region of 375 cm^{-1} as well as 640 cm^{-1} corresponds to Ni-doped MnO_2 octahedra within a tetragonal framework.[43,44] Remarkably, the intensity variation and peak shift (640 cm^{-1}) are found in 8Ni and 10Ni-MnO_2 materials. This suggested that the strengthening of the Mn-O bond and effective replacement of K^+ by Ni^{2+} cations in the α-MnO_2 tunnel structure. These results are in good agreement with the previous reports.[45,46]

10.1002/celc.202101303

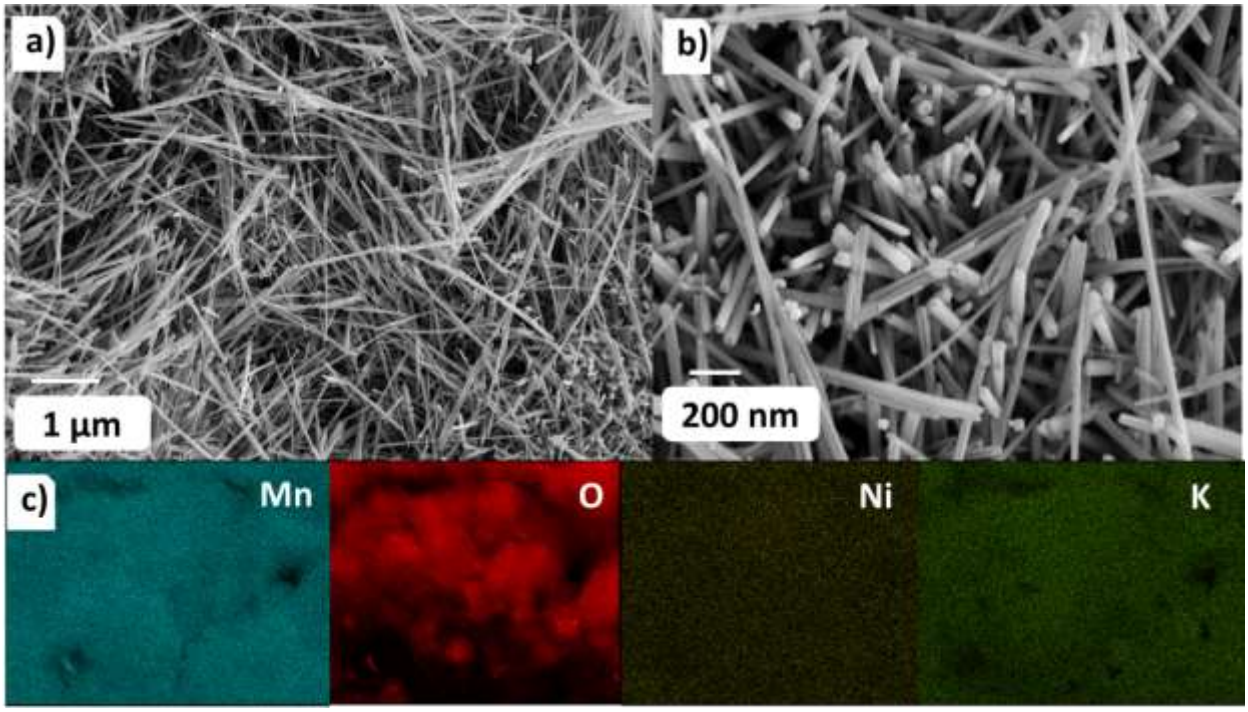

Figure 2. (a, b) FE-SEM low and high magnification images of 8Ni-MnO_2 catalyst, (c) EDAX mapping results of 8Ni-MnO_2 catalyst.

The FESEM image shows the presence of homogeneous nanowires with few microns length, and the various amounts of Ni doping do not affect the morphology of the nanowire catalysts (**Figure 2a, b**). The EDAX elemental mapping result confirms the presence of Mn, O, Ni and K elements in material and that validates they are distributed uniformly throughout the 8Ni-α-MnO_2 nanowire (**Figure 2c**). **Table S2** reveals the atomic concentration of Ni ions increases with increasing the loading amount of $NiSO_4$ precursor. Such observation could be the direct evidence for the Ni doping in α-MnO_2 framework greatly altered by the nickel precursor concentration.

The TEM images of 8Ni-doped MnO_2 confirm the uniform formation of micron size nanowires and their width is around 50-100 nm (**Figure S2**). The corresponding lattice fringes

image of d-spacing value is 0.29 nm well-matched with XRD results calculated for (310) plane. Further, 8Ni-MnO_2 sample exhibit well-developed spots in the SAED pattern attributed to the polycrystalline nature of doped MnO_2 sample. This result indicates that the synthesis process offers phase pure Ni-doped-MnO_2 nanowire samples with effective incorporation of Ni without affecting the nanowire morphology.[40]

Figure S3 represents the XPS spectra recorded for Ni-doped α-MnO_2 nanowire catalyst prepared in this work. The Mn 2p spectrum (**Figure S3a**) demonstrates two major peaks at 642.6 and 654.3 eV are belongs to Mn $2p_{3/2}$ and Mn $2p_{1/2}$ respectively,[47,48] which are the characteristic peaks of α-MnO_2.[45] The observed spin energy separation value (ΔE) of 11.8 eV indicates the predominant oxidation state is Mn^{4+} present in MnO_2 nanowires. From the Mn 3s spectra (**Figure S3b**) one could distinguish the surface oxidation state present in various Ni-MnO_2 materials with respect to concentration of Ni doping. It contains two peaks as a result of coupling between Mn 3d valence electron with non-ionised Mn 3s electron. Ni 2p spectra (**Figure S3c**) illustrate the major peak at 855 eV attributed to the Ni $2p_{3/2}$, signifying the successful doping of Ni^{2+} cation in the tunnel structure.[49] Remarkably, the peak intensity of Ni $2p_{3/2}$ also improved with respect to doping of different concentration of Ni cation, indicating the strongly tuned structural properties of MnO_2.

The splitting value (ΔE Mn 3s) between two peaks is considered as the Mn oxidation state in the catalyst. In this study, we observed different ΔE Mn 3s values of 4.69, 4.72, 4.63 and 4.73 eV for 5Ni-MnO_2, 8Ni-MnO_2, 10Ni-MnO_2 and 15Ni-MnO_2 catalyst, respectively (**Table S2**). From the observed ΔE values, we are able to calculate the average oxidation state (AOS) using the following formula AOS = 8.956 – 1.126 ΔE 3s.[42] The obtained AOS for various

10.1002/celc.202101303

samples are 3.67 (5Ni), 3.64 (8Ni), 3.74 (10Ni) and 3.63 (15Ni-MnO_2)**.** This observation clearly indicates that the doping of Ni cation in the lattices of α-MnO_2 nanowire catalyst greatly alters the AOS and which in turn enhances the Mn^{3+} quantity in the material. It is proposed that cation doping is one of the efficient ways to manipulate the ratio of Mn^{3+}/Mn^{4+}[28] and improves catalytic bifunctional activity. Accordingly, we adopted a metal cation impregnation method to alter the surface properties by occupying the interstitial positions of [2 × 2] tunnels of α-MnO_2 materials. Such an insertion of divalent metal cation in the tunnels would alter the charge balance in the MnO_2 octahedra. It is understood that a fraction of Mn^{4+} in MnO_2 will convert to Mn^{3+} to keep the electroneutrality in the MnO_2 octahedra which eventually raises the Mn^{3+} quantity.

The O 1s scan shows (**Figure S3d**) the two major contributions in the deconvoluted spectrum at 529.9 eV and 531.3 eV which correspond to O^{2-}, OH^-/H_2O respectively.[50] It is worth to mentioning here that Wu *et al*.[51] employed $Ni(NO_3)_2$ along with MnO_2/C in the presence of $NaBH_4$ in order to obtain Ni doping in MnO_2 material. However, they lead to the formation of a mixture of NiOOH, $Ni(OH)_2$ along with MnO_2 material. However, our proposed method will selectively incorporate Ni^{2+} without forming any other hydroxide or oxide species. In addition, our observation testifies that an incremental Ni^{2+} content has evidently modified the electronic properties of MnO_2 which would lead to improved catalytic activity.

2.2 Electrochemical analysis of Ni doped α-MnO_2 materials

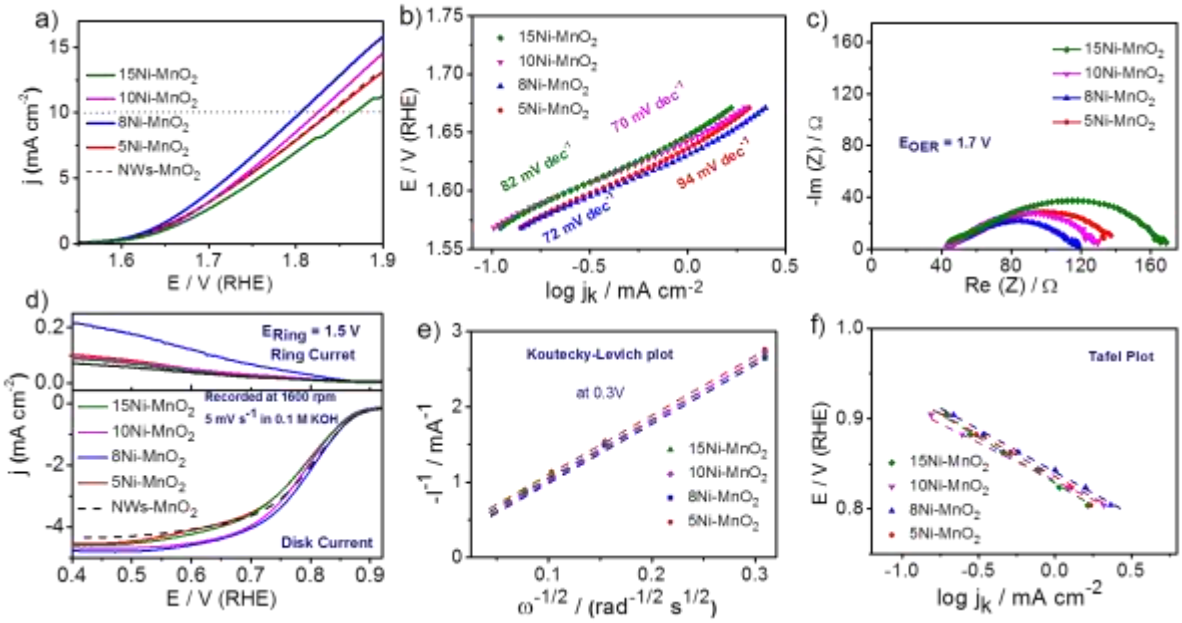

Figure 3. OER and ORR properties of various concentrations of different materials were measured at KOH solution at an electrode rotation speed of 1600 rpm. (a) LSV analysis (scan rate of 5 mV s^{-1}), (b) Tafel plot calculated from LSV analysis, (c) Nyquist plot obtained from EIS measurements at 1.7 V. (d) Disk and ring current performances (ORR) of synthesized materials at 5 mV s^{-1} scan rate, (e) Koutecky-Levich (K-L) plot and (f) Tafel plot analysis for various materials as mentioned in the figure.

Electrocatalytic OER activities of LSV curves of Ni-doped α-MnO_2 materials were demonstrated in **Figure 3a**. The measurement has been made at 1600 rpm and 5 mV s^{-1} scan rate in 0.1 M KOH by employing a rotating disk electrode (RDE). The OER polarization curve depicts the OER getting started at ~1.6 V (onset) and increasing gradually along with the potential, and attains the 10 mA cm^{-2} current density values around 1.84 to 1.87 V *vs* RHE. We have noticed that a little activity difference between undoped NWs-MnO_2 and 5Ni-MnO_2 catalysts. However, when compared to the Ni-MnO_2 catalyst, 8Ni-MnO_2 could observe a significant improvement in OER activity. At the same time, the OER performance decreases for

10Ni-MnO_2 catalyst and it further decreases for 15Ni-MnO_2 catalyst as well. Among the set of catalysts, 8Ni-MnO_2 shows excellent OER activity and it touches the 10 mA cm^{-2} current density at a minimum overpotential of 1.81 V. This observation indicated the Ni^{2+} cation doping can effectively modify the OER activity than undoped MnO_2 nanowire (NWs-MnO_2) material. **Figure 3b** shows the Tafel plot derived from the LSV curve and corresponding slope values are listed in **Table S3**, and is around 70-94 mV dec^{-1} for various xNi-MnO_2 materials. The lower Tafel slope value of the 8 and 10 Ni-MnO_2 implies the fast electron transport and excellent kinetics of OER and our observation is in good agreement with the recent report for Ca, Ag-doped MnO_2 catalyst.[52]

It is interesting to note that the observed OER activity is greatly influenced by the average oxidation state calculated for each xNi-α-MnO_2 catalyst. For example, the AOS calculated for the 8Ni-MnO_2 material was 3.64, which is due to the highest fraction of Mn^{3+} present in the material. It has been previously reported that surface Mn^{3+} species present in MnOx catalyst act as an active site for OER which leads to a significant decrease of the overpotential. It could be clearly seen from our XPS results that the fraction of the Mn^{3+} present in 8Ni-MnO_2 is the key factor which enhances the OER activity. **Figure 3c** represents the EIS spectrum (Nyquist plot) measured at 1.7 V for various materials. It is used to calculate the charge transfer resistance (R_{ct}) of the catalyst material under OER condition. Interestingly, the 8Ni-MnO_2 catalyst also exhibits a lower R_{ct} value (75 Ω cm^{-2}) than that of other materials (85-127 Ω cm^{-2}). Further to evaluate the intrinsic activity of the Ni-MnO_2 catalyst, TOF values and mass activities were calculated and given in **Table S3**. Lower TOF (1.42 X 10^{-2} s^{-1}) and higher mass activity (62.3 A g^{-1}) were also detected in 8Ni-MnO_2 material, indicating excellent activity toward OER.

The ORR polarization curve (**Figure 3d**) describes that the onset of reduction current begins at ~0.9 V for Ni-doped MnO_2 nanowire catalyst and gradually improves then travels via a mixed kinetic and diffusion controlled at 0.7 to 0.5 V, and finally reaches a plateau mass-transfer control at around 0.5 V. We observed appreciable oxygen reduction activity for four xNi-MnO_2 nanowire catalysts, among them 8Ni-MnO_2 catalyst shows the maximum activity based on its more positive onset of 0.89 V, $E_{1/2}$ value of 0.79 V and it reaches a current density of 3 mA cm^{-2} at minimum over potential value of 0.77 V. **Figure 3e** and **f** show the corresponding K-L and Tafel plots drawn from the ORR-LSV curves, respectively. The K-L plot demonstrates the excellent linear behaviour that indicates the first-order kinetics of ORR.[53,54]

Further to evaluate the ORR activity of the Ni-doped catalyst, the calculated electron transfer value (n-value), mass activities, amount of H_2O_2 produced and rate constant values are presented in **Table S4**. The n-values obtained from the slope of the K-L plot at 0.3 V, confirm the close to four-electron reduction pathway as that of Pt/C. Besides, acquired peroxide species of Ni-doped materials are 9-23 %. This finding suggests that single doped MnO_2 materials were able to reduce O_2 to OH^- through a direct four-electron reduction reaction, affords superior ORR efficiency. Moreover, the Tafel plot provides kinetic evidence for ORR, for Ni-MnO_2 materials, the slope value of 92-98 mV dec^{-1} signifying the more favourable ORR kinetics (**Figure 3f**).[55] In addition, 8Ni-MnO_2 shows the highest mass activity (23.2 A g^{-1}) and rate constant values (1.95 x 10^{-2} cm s^{-1}) than that of other materials and is almost close to the benchmark material. It is worth to compare the rate constant of 8Ni-MnO_2 sample with 2.92% Cu-doped α-MnO_2 nanowires reported by Davis *et al*.[56] They observed a value of k_{chem} = 1.9 x 10^{-2} cm s^{-1} for Cu-doped -α-MnO_2 nanowires which is in good agreement with our value of 1.95 x 10^{-2} cm s^{-1} under similar experimental conditions.

10.1002/celc.202101303

It is worth to mention here that the Ni-doping into the lattices of α-MnO_2 nanowire material (8Ni-MnO_2) retains its efficient ORR activity even though it possesses a lower average oxidation state of 3.64 and an excess of 3+ quantity of Mn which promoted OER significantly. The 8Ni-MnO_2 catalyst stands as the superior catalyst based on its lower overpotential (1.81 V) to reach 10 mA cm^{-2}, Tafel slope value of 72 mV dec^{-1} and lower Rct value of 75 Ω cm^{-2} towards OER. Similarly, on the ORR side it has the merits of larger half-wave potential (0.79 V), highest n-value (3.5) and an average Tafel slope value of 94 mV dec^{-1}. Therefore, we selected the 8Ni-MnO_2 catalyst for further dual-doping with Co^{2+} cations to evaluate the bifunctional activity.

2.3 Cobalt and Nickel cations co-doping into α-MnO_2 Nanowires

The effect of single Ni doping with various concentrations resulted in 8Ni-MnO_2 exhibiting excellent OER and ORR activity attributed to their high concentration of Mn^{3+} and Mn^{4+} respectively. Therefore, we fixed 8Ni-MnO_2 for dual doping analysis. Here, we employed a $CoSO_4$ precursor for Co^{2+} cation secondary doping at various concentrations such as 5, 8, and 10 mmol to systematically analyze the OER/ORR activity. Initially, we prepared 8Ni-MnO_2 nanowire materials followed by Co^{2+} cation was selectively incorporated into the tunnel structure by replacing K^+ cation only without modification of nanowire morphology.

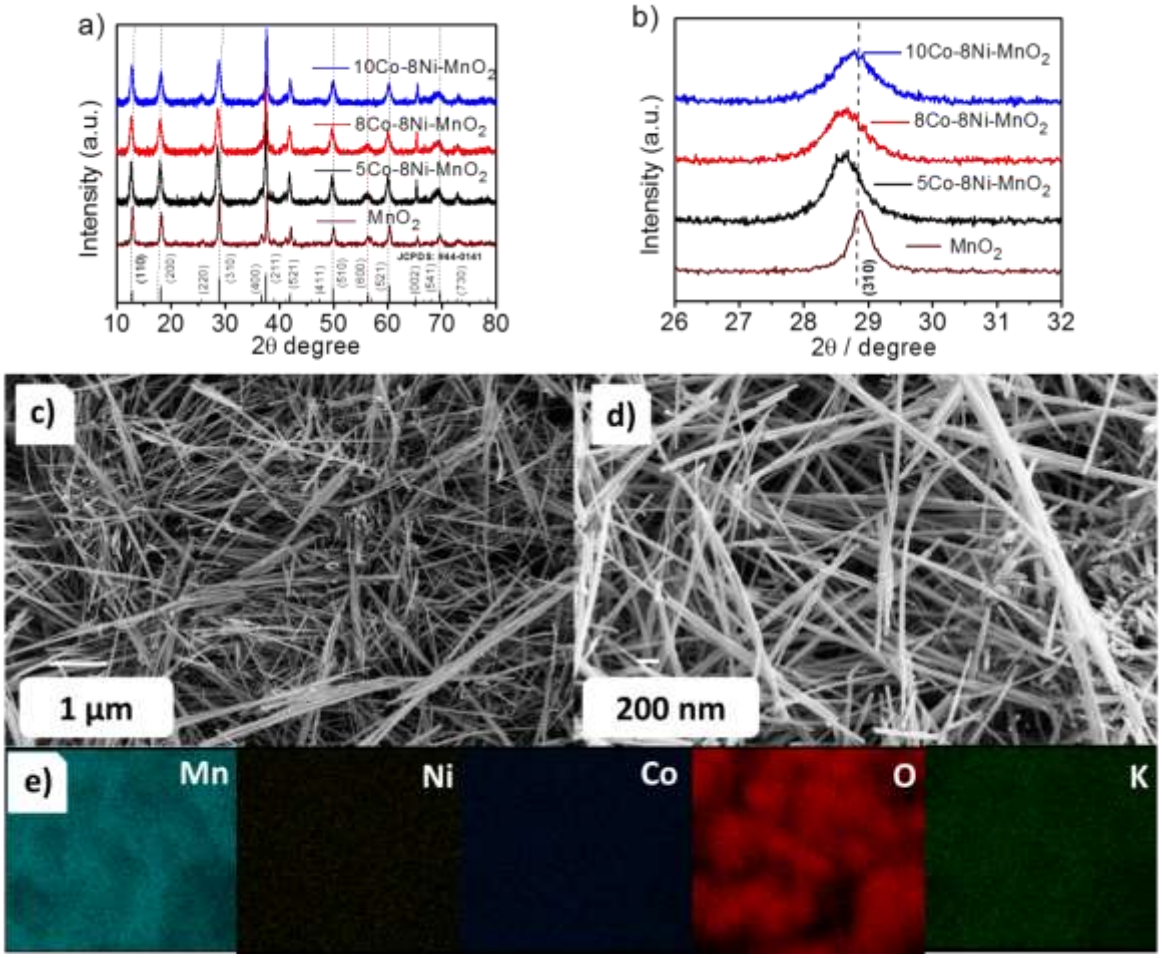

Figure 4. (a) XRD patterns of various loading of dual cation doped MnO_2 materials. (b) Enlarged view of (310) plane shows peak shift and peak broadening in XRD pattern. (c, d) FESEM morphology and (e) EDAX mapping results of 8Co-8Ni-MnO_2 catalyst.

Further, the crystalline nature of dual doped products are confirmed by the XRD pattern (**Figure 4a**).The obtained 2θ diffraction peaks at 12.7, 18.1, 28.8, 37.5, 41.9, 49.8, 56.2, 60.2, and 69.7^o are well-matched with JCPDS pattern no 44-0141. The peak broadening and peak shift was found in the prepared nanowires revealed differences in their crystal dimension (**Figure 4b**). These results suggest that the doping of cobalt into the Ni-MnO_2 lattice without altering the crystal structure.[57] There is no sign of any impurity phases other than the α-MnO_2 phase in the prepared material. It offers strong evidence that Ni and Co are incorporated as ions in the crystal

lattice of α-MnO_2 materials. Further, we calculated FWHM, d-spacing and crystallite size (D) values of synthesized materials were demonstrated in **Table S5**. The reductions of (310) plane of d spacing value and crystallinity were certified to the presence of Co^{2+} cation in the channels.

In the FTIR spectra of dual doped MnO_2 materials, three peaks are generally perceived to be attributed to the Mn-O bond of octahedral sites (**Figure S4a**). The high-frequency peaks at 466 and 520 cm^{-1} are assigned to the stretching mode of the Mn-O bond which approves the formation of MnO_2 octahedral tunnel structure (MnO_6). The low-frequency peak at 716 cm^{-1} corresponds to the stretching vibration of the Mn-O bond in tetrahedral sites.[58] **Figure S4b** portrays the Raman spectra of cation doped materials. In Raman spectra, the major peak at 640 cm^{-1} corresponds to Mn-O symmetry stretching vibration in the MnO_2 framework. This peak is attributed to the A1g symmetry mode and space group of C_{2h}. The low-intensity peak at 571 cm^{-1} is the fingerprint for the Mn-O stretching vibration of MnO_6 groups.[46] Similarly, the low-intensity peaks at 345 and 180 cm^{-1} are indexed to the MnO_2 octahedra framework. Interestingly, 8Co-8Ni-MnO_2 exhibits a low-intensity peak at 640 cm^{-1} compared with other samples, which point out the dual doping creating more defect sites which are greatly involving the OER and ORR to increase the activity.

The distribution of divalent cations of nickel and cobalt in the prepared materials are investigated in FESEM analyses are presented in **Figure 4c** and **d** which confirmed the successful formation of proposed nanowire structure. Further, doping of Co^{2+} cation on Ni-MnO_2 similar nanowire morphology was retained, which confirms the successful replacement of K^+ cation by hydrothermal approach. FESEM EDX analysis is used to confirm a uniform distribution of Mn, Ni, Co, O and K on the nanowire, representing the effective doping of metal ions (**Figure 4e**). Meanwhile, atomic concentrations of doping ions were probed by FESEM

10.1002/celc.202101303

EDX mapping is listed in **Table S6**. The exchange of K^+ by metal cations is confirmed by the increase in the cobalt atomic concentration from 0.67 to 1.02 % and simultaneous decreases of K^+ concentration in nanowire structure.

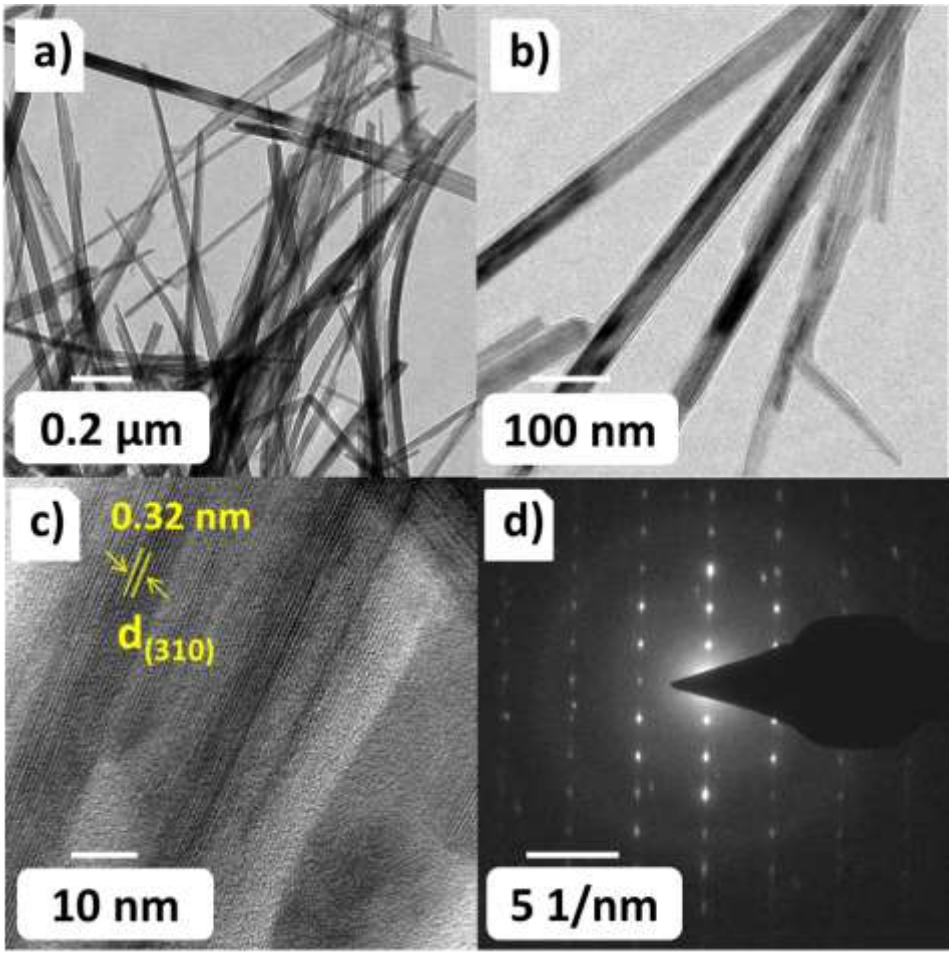

Figure 5. TEM morphology of 8Co-8Ni-MnO_2 catalyst: (a-b) Low and high magnified images, (c) lattice fringes and (d) its corresponding SAED pattern.

The nanowire morphology and crystalline structure of dual doped materials further examined by TEM analysis are given in **Figure 5**. The 8Co-8Ni-MnO_2 sample display a uniform nanowire morphology with several nm size. Their respective fringes and SEAD patterns are also displayed in **Figure 5 c** and **d**. The d-spacing value of 0.32 nm has been calculated from the

fringes and its good agreement with XRD (310) plane. In addition, well-ordered diffraction rings with uniform spots are observed in the SAED pattern owing to their polycrystalline nature of dual doped materials.

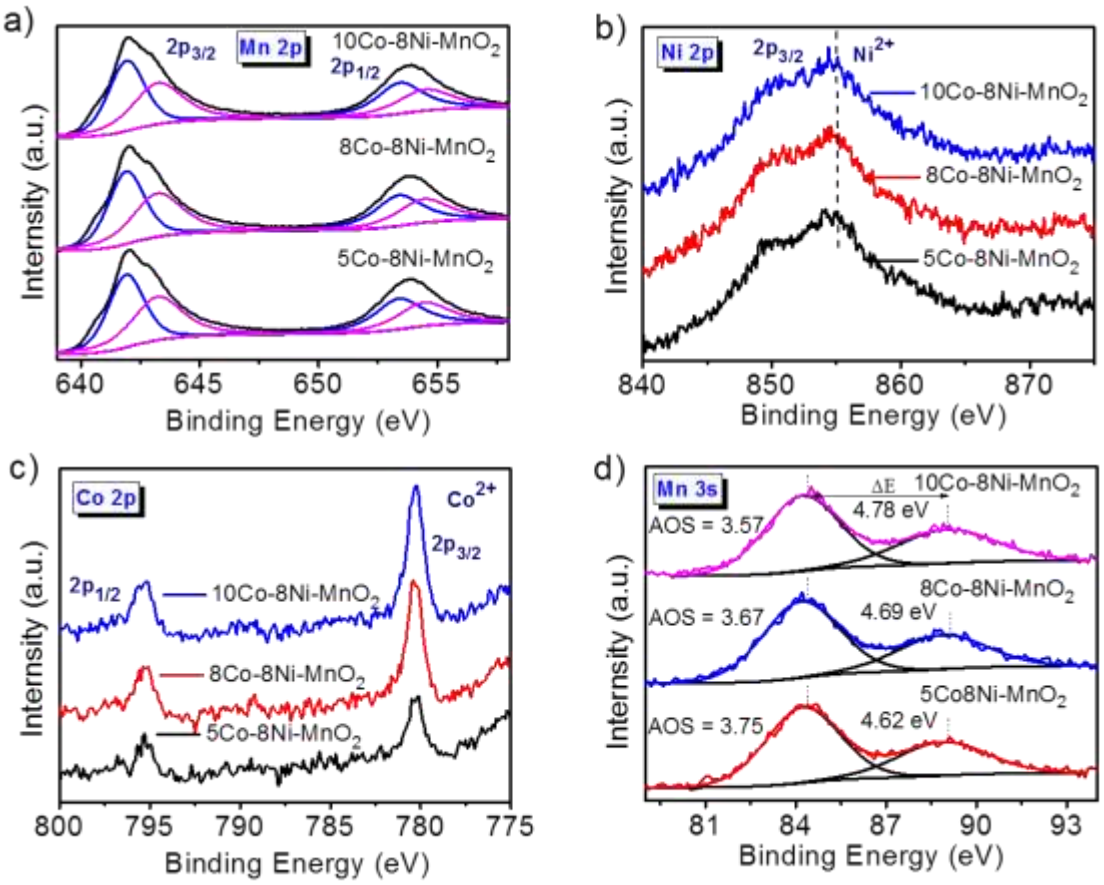

Figure 6. High-resolution XPS spectra of (a) Mn 2p, (b) Ni 2p, (c) Co 2p and (d) Mn 3s for 5Co-8Ni-MnO_2, 8Co-8Ni-MnO_2 and 10Co-8Ni-MnO_2 materials.

Generally, the Mn^{3+} state of MnO_2 materials are highly active than MnO_X, whereas Mn^{3+} sites in the MnO_6 octahedra tunnel structure are highly unstable. As a result, it readily absorbs the OH species and converts MnOOH intermediates, hastening the OER. Further, metal cation, specifically divalent cation in MnO_6 octahedra tunnel structure stimulates effectively both the

OER and ORR activity due to alteration of few Mn^{4+} into Mn^{3+} sites. Consequently, the chemical nature and oxidation states of different elements in the Co-8Ni-α-MnO_2 nanowires catalyst are analyzed by XPS spectra. The wide scan spectrum point out the availably of transition metals including Ni, Co, Mn and other elements (O and K) in the nanowire framework (**Figure S5**). The Mn 2p scan displays two peaks at the binding energies of 642 and 654 eV for Mn $2p_{3/2}$ and Mn $2p_{1/2}$ respectively (**Figure 6a**).[59,60] The presence of Ni 2p peak at ~852 eV confirms the manifestation of Ni^{2+} ions in the channel (**Figure 6b**). Similarly, the Co 2p XPS spectrum of **Figure 6c** Co 2p displays a doublet at 781 and 796 eV owing to Co^{2+} with a spin energy separation of 15 eV, proposing the successful doping of Co^{2+} cation into the octahedral framework.[61] The presence of both Ni^{2+} and Co^{2+} ions are in good agreement with the observed EDAX results.

Subsequently, Mn 3S peak separation (ΔE) values are additional evidence that MnO_2 nanowires materials are in the Mn^{4+} oxidation state (**Figure 6d**). The observed ΔE values for 4.62 (5Co), 4.69 (8Co), and 4.78 (10Co-8Ni-MnO_2) respectively. Similar results are reported by Lubke *et al*.[62] Moreover, AOS is calculated from the ΔE Mn 3s spin-orbit value as discussed in the previous section. Ni and Co dual doping in MnO_2 nanowire also exhibits a decreasing trend in AOS with an increase in Co doping testifies the surface enrichment of 3+ oxidation state of Mn in the material. Here, the decrease in AOS indicates the improvements of OER active sites such as Mn^{3+} suggested the doping effect. Similarly, Mn^{4+} active sites are accountable for decreasing the O-O bond strength and leading to reduction of activation energy to improve the ORR. Dual doping significantly enhances the synergistic effects in MnO_2 framework which are initiated by strong electrical and chemical coupling reactions and subsidize the bifunctional activity. The O 1s scan has two main contributions in the deconvoluted spectrum at 529.6 eV,

531.5 eV are corresponding to O^{2-} and OH^{-}, respectively (**Figure S6**).[63] According to the above results, the divalent cations (Ni^{2+} and Co^{2+}) are effectively replaces the K^{+} ions in the octahedra [MnO_6] units thereby generating Mn^{3+} valence sites in the material.

2.4 Oxygen Evolution Reaction Studies on dual doped MnO_2 materials

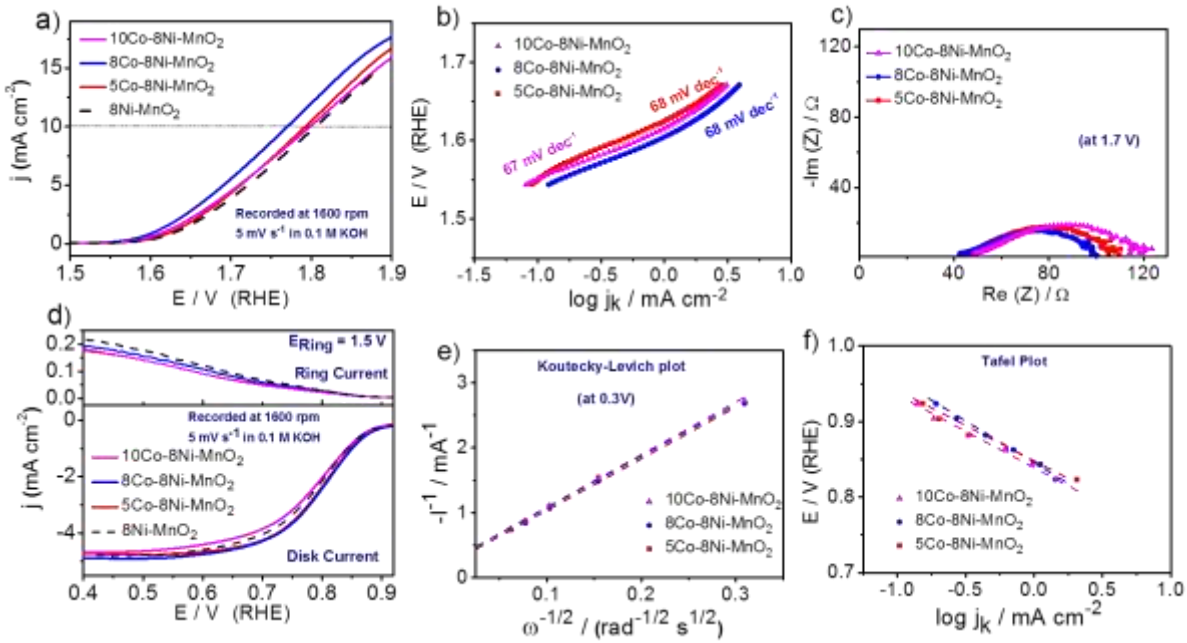

Figure 7. (a) OER-LSV analysis of 5Co-8Ni-MnO_2, 8Co-8Ni-MnO_2, and 10Co-8Ni-MnO_2 materials were measured at 0.1 M KOH solution with a scan rate of 5 mV $s^{-1}$and electrode rotation speed of 1600 rpm. (b) Tafel plot derived from LSV analysis, (c) Nyquist plot of the EIS for various doped materials measured at 1.7 V. (d) Representative disk and current curves (ORR) of prepared materials measured at a scan rate of 5 mV s^{-1} and with 1600 rpm. (e) Koutecky-Levich plot of synthesized materials were performed at 0.3 V. (f) Mass transfer corrected Tafel plot for various materials as mentioned in the figure.

The OER polarization curve (**Figure 7a**) shows the onset current starts at ~1.6 V and increases with the applied potential. The OER potential to reach 10 mA cm^{-2} for the 5Co-8Ni-MnO_2, 8Co-8Ni-MnO_2 and 10Co-8Ni-MnO_2 electrodes were 1.79, 1.77 and 1.80 V respectively (**Table S7**). These values are significantly lower than that of single doped catalysts. The observed activity is higher for 8Co-8Ni-MnO_2 when compared with other doped catalysts. This could be related to the optimum concentration of Co^{2+} doping triggering the larger extent of Mn^{3+} cations which improves the OER performance. This outcome confirms that the enhanced OER activity resulted from optimum doping concentration of Co^{2+} in the Ni-doped MnO_2 framework, along with an increase in the Mn^{3+} state, and improved active sites.[64,65]

The Tafel plot derived from the LSV data and their linear fittings are shown in **Figure 7b.** The lower Tafel slope values are perceived in 8Co-8Ni-MnO_2 materials (~ 68 mV dec^{-1}) which are relatively lower than of Ni-MnO_2 materials (70-94 mV dec^{-1}) and RuO_2 (82 mV dec^{-1}) (**Table S7**). This observation are in very good agreement with the Tafel value of 57 mV dec^{-1} for MnO_2-Co (7.6%) and 62 mV dec^{-1} for MnO_2-Ru (9.4%) doped catalyst reported by Lubke et al.[62] These results suggest that the synthesized cobalt-nickel doped nanowire materials are highly favorable for improved kinetics and catalytic activity. Further, to clarify the electronic effect of Co-Ni-MnO_2 catalysts the EIS analysis are performed and presented (**Figure 7c)**. All the Co-Ni-MnO_2 electrodes established smaller curvature with R_{ct} values of 57-80 Ω cm^{-2}, proposing an outstanding electron transfer activity at the interface. Moreover, higher TOF and mass activity were displayed by 8 Co-Ni-MnO_2 than other materials (**Table S7**). Based on these parameters, 8Co-8Ni-MnO_2 catalyst stands superior to other catalysts prepared. These results indicate that dual cation doping improves the conductivity of pure α-MnO_2 materials and facilitates a decrease in the overpotential for OER.

2.5 Oxygen Reduction Reaction Studies on dual doped MnO_2 materials

The LSV-disk current curve shows (**Figure 7d**) the ORR happens at ~0.9 V at the Co-8Ni-doped nanowire catalyst surface and passes through the mixed control region at 0.7 to 0.5 V. Further, it touches a plateau region at a potential of 0.5 V. The more positive onset potential was found in 8Co-8Ni-MnO_2 material than others. Likewise, the detected half-wave potential and current density values are summarized in **Table S8**. From the table, we observed appreciable activity for three xCo-8Ni-MnO_2 nanowire catalysts. Notably, the 8Co-8Ni-MnO_2 catalyst shows remarkable activity based on its $E_{1/2}$ value (0.80 V) and it reached a current density of 3 mA cm^{-2} at a minimum over potential value of 0.77 V. These values are almost close to Pt/C catalyst of $E_{1/2}$ (0.84) and overpotential (0.81 V) values.[66,67]

Figure 7e reveals the corresponding K-L plot assessed from the disk current values observed at 0.3 V. The excellent linearity of the K-L plot was a witness for first-order kinetics with respect to O_2. According to K-L analysis, the total current density of dual doped MnO_2 electrodes can be estimated from the following equation.[68]

$$\frac{1}{J} = \left(\frac{1}{j_k}\right) + \left(\frac{1}{j_d}\right) ----\rightarrow 1$$

Where j_d and j_k is related to the kinetic current density and diffusion current density respectively.

The ORR efficiency is mainly correlated with the n-values. Therefore, we calculated the n-value by using the K-L equation (equation, 2).[36,68]

$$j_d = 0.62\, nFC\mathrm{D}^{\frac{2}{3}} v^{-\frac{1}{6}}\, \omega^{\frac{1}{2}} ----\rightarrow 2$$

in which the F and C correspond to the Faraday constant (96485 C mol^{-1}) and concentration of oxygen (1.21×10^{-6} mol cm^{-3}) in electrolyte solution respectively. D and ν are the diffusion coefficient (1.85 X 10^{-5} cm^2 s^{-1}) and kinematic viscosity of alkaline electrolyte respectively. ω describes the angular velocity. During the oxygen reduction performance, the production of peroxide (HO_2^-) species are estimated by ring electrode performance and keeping potential at 1.5 V (equation 3).[68]

$$\% \, HO_2^- = \frac{200\left(\frac{I_R}{N}\right)}{I_D + \left(\frac{I_R}{N}\right)} ----\rightarrow 3$$

In ORR, the calculated n value to be 3.4, 3.5 and 3.4 on 5Co-8Ni-MnO_2, 8Co-8Ni-MnO_2 and 10Co-8Ni-MnO_2 respectively, the similar value was perceived in Pt/C. This result reveals that all the materials followed a closed four-electron reduction mechanism toward ORR. At the same time, the formation of HO_2^- was recognized as an intermediate product which produced during a step-wise two-electron transfer process.[69] The estimated peroxide yields are 19, 20 and 20% for 5Co-8Ni-MnO_2, 8Co-8Ni-MnO_2 and 10Co-8Ni-MnO_2 respectively (**Table S8**), revealing that the 8Co-8Ni-MnO_2 catalyst confirmed the better activity than others. Further, electrode kinetics studies were evaluated by mass-transfer corrected Tafel plot was presented in **Figure 7f**. Tafel plot was drawn from the j_k of K-L plot intercept of different applied potential values. All the electrode materials showed smaller Tafel slope values (88-95 mV dec^{-1}), implying the faster kinetics of ORR.

$$j_k = nFk_{chem}C ----\rightarrow 4$$

Additionally, rate constant (k_{chem}) value and mass activity also responsible for ORR performance is presented in **Table S8**.[70] The k_{chem} was measured by i_k value (equation 4) which is obtained

10.1002/celc.202101303

from the K-L plot intercept. The values of k_{chem} for 1.83 (5Co), 1.94 (8Co) and 1.78 x 10^{-2} cm s^{-1} (10Co-8Ni-MnO_2) respectively. The mass activity was measured at 0.3 V and the values for 22.9 (5Co), 23.6 (8Co) and 22.8 A g^{-1} (10Co-8Ni-MnO_2) respectively. Among them, 8Co-8Ni-MnO_2 shows the highest rate constant and mass activity values towards ORR in the alkaline solution.

In conclusion, our experimental result proves that bi-cation doping of Ni and Co significantly improved both the OER and ORR activity of α-MnO_2 nanowire material. Ni and Co dopant ions play a vital role which leads to a synergistic effect in enhancing intrinsic conductivity and lowering the crystal domain size. Based on the XRD and Raman analysis, we inferred that there were no changes in the crystal structure after co-doping of Ni and Co ions. Interestingly, both the Ni and Co dual dopants successfully retain the [2 x 2] tunnel structure of the α-MnO_2 nanowire and increase the fraction of Mn^{3+} ion and thereby a decrease in average oxidation sate has been observed for the doped material. Such an observation leads to a decrease in OER overpotential and an enhancement in TOF. In addition, the Ni and Co dual doping demonstrates a comparable activity towards both OER and ORR with the previously reported mono and dual doped MnO_2 catalyst material as shown in **Table 1**.

10.1002/celc.202101303

Table 1. Catalyst performance comparison of prepared catalysts with previous literature.

Catalysts	OER		ORR	ΔE (E_{OER}@10 mA cm^{-2} - ORR@$E_{1/2}$)	Reference
	E (V/RHE) (j@10 mA cm^{-2})	Tafel slope (mV dec^{-1})	$E_{1/2}$ (V/ RHE)		
α-MnO_2-Ca-Ag	~1.77 (~0.77 *vs* Ag/AgCl)	-	-	-	[43]
α-MnO_2-Cu (2.9%)	-	-	0.71 (~ -0.29 *vs* Ag/AgCl)		[56]
MnO_2-Co (7.6%)	~1.84 (~0.84 *vs* Ag/AgCl)	57	0.720 (~ -0.28 *vs* Ag/AgCl)	~ 1.08 V	[62]
MnO_2-Ru (9.4%)	~1.73 (~0.73 *vs* Ag/AgCl)	62	0.820 (~ -0.18 *vs* Ag/AgCl)	~ 0.91 V	[62]
α-MnO_2 –Ru (MR20)	1.64	-	~0.82	0.82 V	[71]
α-$Mn_{0.9}Co_{0.1}O_2$	(~0.64 *vs* SCE)	-	(~ -0.21 *vs* SCE)	0.85 V	[72]
α-MnO_2	1.84	-	0.79	1.05 V	This work
8Ni-MnO_2	1.81	72	0.79	1.02 V	
8Co-8Ni-MnO_2	1.77	68	0.80	0.97 V	

2.6 Bifunctional activity of materials

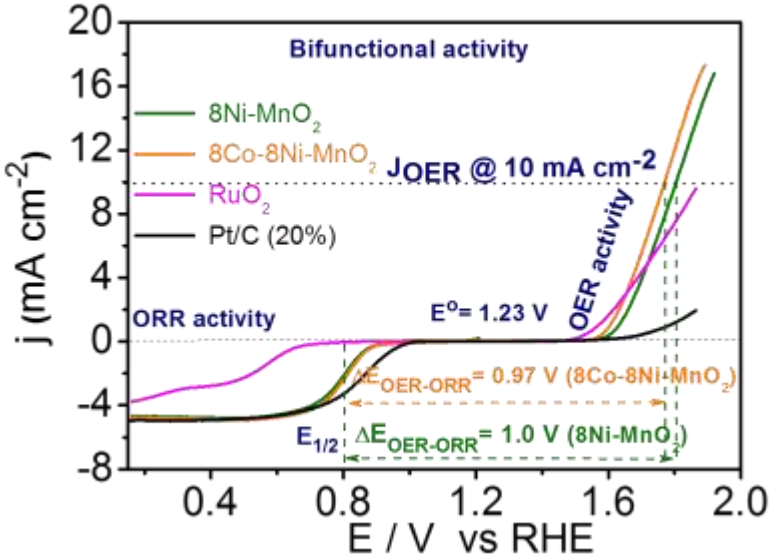

Figure 8. (a) Comparison of the bifunctional activity of 8Co-8Ni-α-MnO_2 with benchmark catalysts.

The bifunctional activity (**Figure 8**) is the measure of potential difference (ΔE) between the OER at 10 mA cm^{-2} and ORR at its $E_{1/2}$ value (ΔE = E_{OER}@10 mA cm^{-2} - ORR@$E_{1/2}$). The lower ΔE value is an indication of good bifunctional activity of the catalyst. The above LSV curve demonstrates the bifunctional activity of 8Ni-MnO_2 and 8Co-8Ni-MnO_2 catalyst posses the ΔE value of 1.02 V and 0.97 V respectively. The above observations suggest that the bifunctional catalytic activities are more facile on 8Ni-MnO_2 catalyst (in the case of mono dopant) and 8Co-8Ni-MnO_2 (bi-dopant) catalyst nanowires obtained. In the case of 8Co-8Ni-MnO_2 material which induces a raise in Mn^{3+} quantity thereby creates new active centers for water adsorption and enhances the OER effectively. At the same time a small reduction in Mn^{4+} active sites retains similar ORR activity.

3. Conclusions

A series of mono and bi-cation doped manganese oxide nanowires were synthesized by a simple hydrothermal process. Comprehensive material analysis proved that there were no changes in the α-MnO_2 crystal structure and morphology after doping of Ni and Co ions. Ni and Co ions play an important role which leads to a synergistic effect in enhancing intrinsic conductivity as well as lowering the crystal domain size. In addition, Ni and Co dual doping significantly increased the fraction of Mn^{3+} quantity which has been proved by the observed average oxidation state. The superior OER and ORR catalytic performance of 8Co-8Ni-α-MnO_2 is demonstrated by electrochemical studies. 8Co-8NiMnO_2 material showed excellent OER activity with a low overpotential (1.77 V at 10 mA cm^{-2}), lower Tafel slope (68 mV dec^{-1}) and R_{ct} value (57 Ω cm^{-2}). Moreover, ORR studies demonstrated a more positive onset potential (0.90 V), half-wave potential (0.80 V), better current density (3 mA cm^{-2} at 0.77 V), lower Tafel slope value (95 mV dec^{-1}) and follow a direct four-electron pathway. In addition, bifunctional activity of single (8Ni-MnO_2) and dual cation (8Co-8Ni-MnO_2) doped material revealed the low overpotential of 1.02 and 0.97 V respectively, designates admirable activity in 0.1M KOH electrolyte solution.

Experimental Section

Materials

Potassium permanganate ($KMnO_4$), manganese sulfate monohydrate ($MnSO_4.H_2O$), nickel (II) sulfate hexahydrate ($NiSO_4.H_2O$), cobalt (II) sulfate heptahydrate ($CoSO_4.7H_2O$) were purchased from Merck. These are used to synthesis the Ni and Co dual doped of α-MnO_2

materials. Further, potassium hydroxide (KOH) pellets were obtained from Merck and the Nafion solution purchased from Sigma Aldrich which was directly used in electrochemical OER and ORR analysis.

Synthesis of Ni-doped α-MnO_2 (Ni-MnO_2) nanowire material

Different amounts of doping of nickel ion into the α-MnO_2 nanowires were attained by the hydrothermal synthesis process as follows. Four different ratios of $NiSO_4$ such as 5, 8, 10, 15 mmol were added into the 30 mL of 0.507 g of $MnSO_4$ and 0.475 g of $KMnO_4$ (0.1 : 0.1 mol) α-MnO_2 nanowire precursor composition and made as a homogenous mixture. The obtained mixture was transferred in a 50 mL autoclave and heated separately at 140 ^oC for 24 h. Finally, the solid Ni-MnO_2 products were collected by centrifugation at 4000 rpm and washed with Millipore water/ethanol solvents and dried at 60 ^oC for overnight. Then the collected products were labelled as 5, 8, 10 and 15 Ni-MnO_2 respectively.

Synthesis of Ni and Co-doped α-MnO_2 (Co-Ni-MnO_2) nanowire materials

By using a similar synthesis approach, we followed the preparation of Co-Ni-MnO_2 nanowire, and additionally added three different ratios of $CoSO_4$ (5, 8, 10 mmol) in a fixed volume of 8Ni-MnO_2 separately. Finally, obtained Co and Ni dual doped MnO_2 products were named as 5, 8, and 10Co-8Ni-MnO_2 respectively.

Characterization of α-MnO_2 materials

The crystalline nature of Co and Ni-doped α-MnO_2 materials were confirmed by Bruker D8 advance model powder X-ray diffractometer working at 40 kV and recorded ranges of 10-90° with Cu source. The octahedral and tetragonal tunnel structure of α-MnO_2 samples were

10.1002/celc.202101303

inspected by Raman spectra with LabRAM HR evolution Horina Jobin Yvon and laser excitation wavelength of 532 nm. The Mn bonding sites and functional groups were identified by using fourier-transform spectra (Bruker Optic Gmbh TENSOR 27) recorded transmittance ranges of 40-4000 cm^{-1}. The nanowire morphology and presence of metal atoms in nanowires were examined by Carl ZEISS Germany supra 55 VP Field emission scanning electron microscopy and the operating voltage of 5-30 kV. The nanowire length, morphology and crystalline nature of synthesized materials were investigated by transmission electron microscopy (Tecnai 20 G2) with an accelerating voltage of 200 kV. Dual doped cation, oxidation state and elemental compositions of MnO_2 samples were clearly investigated by MULTILAB 2000 thermo scientific X-ray photoelectron spectroscopy. The Sample preparation and loading methods for characterisation analysis as explained in supporting information section.

Electrochemical Measurements of α-MnO_2 samples

To prepare the α-MnO_2 catalyst ink by the following methods. Initially, 5.6 mm diameter of Glassy carbon (GC) electrode (area = 0.247 cm^2) was polished by using various sizes of alumina suspension solution such as 1, 0.3 and 0.05 µm respectively. Followed by a 6.1 mg of various MnO_2 materials are dispersed in 1 mL of 0.5 % Nafion (0.1 mL of Nafion dissolved 0.9 mL of ethanol) along with Vulcan XC-72 (20%) activated carbon. This catalyst slurry was sonicated for 45 min to form a homogeneous mixture**.** After that, 3 µL of the homogenous ink was drop casted on GC RDE/RRDE surface to achieve a loading of 0.204 mg cm^{-2}. Then it was dried at room temperature for 2 h and employed for OER and ORR analysis.

The electrochemical bifunctional analyses were carried out by using PINE RRDE setup connected to AUTOLAB bipotentiostat PGSTAT 302 N with three-electrode configurations and

NOVA 1.1 software. All the electrochemical analysis was performed in room temperature at 25 ^{o}C. GC electrode was used as a working electrode, Pt as a counter electrode and Ag/AgCl as a reference electrode. For the OER analysis, LSV analyses were recorded at 1600 rpm in 0.1 M KOH electrolyte solution at a scan rate of 5 mV s^{-1}. Potentiostatic EIS Nyquist plot analysis was implemented at 1.66 V *vs* RHE with no electrode rotation in an alkaline electrolyte medium. Prior to ORR analysis, the alkaline electrolyte was saturated with oxygen gas for 30 min. LSV polarization curves recorded with various electrode rotation rates from 100 to 2500 rpm with a scan rate of 5 mV s^{-1} and keeping Pt ring electrode (geometric area = 0.19 cm^2) at 1.5 V *vs* RHE. The electron transfer pathway, percentage of peroxide yields and the mass activity were calculated in the limiting region at 0.3 V *vs* RHE. All the applied potential values of cation doped MnO_2 electrodes were converted to the reversible hydrogen electrode scale by following the formula $E_{RHE} = E_{measured} + E^{o}_{Ag/AgCl} + 0.059$ (pH).

CSIR-CECRI manuscript communication number:

CECRI/PESVC/Pubs./2021-122.

Acknowledgments

We would like to acknowledge Director, CSIR-Central Electrochemical Research Institute (CECRI) for support and encouragement. Selvakumar thanks the financial support through the CSIR-HRDG, New Delhi, India for SRF (grant no. 31/20(159)2k17). The project was supported by Researchers Supporting Project number (RSP-2021/143), King Saud University, Riyadh, Saudi Arabia.

Conflict of Interest

The authors declare no conflict of interest.

Keywords: cobalt doping · manganese oxides · OER/ORR electrode · RRDE · Tafel slope.

References

[1] Y. Tong, P. Chen, T. Zhou, K. Xu, W. Chu, C. Wu, Y. Xie, *Angew. Chemie - Int. Ed.* **2017**, *56*, 7121–7125.

[2] N. H. Kwon, K. G. Lee, H. K. Kim, S. J. Hwang, *Mater. Chem. Front.* **2021**, *5*, 3549–3575.

[3] C. X. Zhao, J. N. Liu, J. Wang, D. Ren, B. Q. Li, Q. Zhang, *Chem. Soc. Rev.* **2021**, *50*, 7745–7778.

[4] W.-H. Li, J. Lv, Q. Li, J. Xie, N. Ogiwara, Y. Huang, H. Jiang, H. Kitagawa, G. Xu, Y. Wang, *J. Mater. Chem. A* **2019**, *7*, 10431–10438.

[5] J. M. Gonçalves, M. N. T. Silva, K. K. Naik, P. R. Martins, D. P. Rocha, E. Nossol, R. A. A. Munoz, L. Angnes, C. S. Rout, *J. Mater. Chem. A* **2021**, *9*, 3095–3124.

[6] C. E. Beall, E. Fabbri, T. J. Schmidt, *ACS Catal.* **2021**, *11*, 3094–3114.

[7] Y. Wang, J. Li, Z. Wei, *J. Mater. Chem. A* **2018**, *6*, 8194–8209.

[8] D. G. Lee, S. M. Kim, H. Jeong, J. Kim, I. S. Lee, *ACS Nano* **2014**, *8*, 4510–4521.

[9] X. He, X. Yi, F. Yin, B. Chen, G. Li, H. Yin, *J. Mater. Chem. A* **2019**, *7*, 6753–6765.

[10] M. R. Benzigar, S. N. Talapaneni, S. Joseph, K. Ramadass, G. Singh, J. Scaranto, U.

Ravon, K. Al-Bahily, A. Vinu, *Chem. Soc. Rev.* **2018**, *47*, 2680–2721.

[11] R. Cheng, F. Wang, M. Jiang, K. Li, T. Zhao, P. Meng, J. Yang, C. Fu, *ACS Appl. Mater. Interfaces* **2021**, *13*, 37123–37132.

[12] H. Zhang, C. Lin, F. Du, Y. Zhao, P. Gao, H. Chen, Z. Jiao, X. Li, T. Zhao, Y. Sun, *ACS Sustain. Chem. Eng.* **2015**, *3*, 2049–2057.

[13] R. Farhat, J. Dhainy, L. I. Halaoui, *ACS Catal.* **2020**, *10*, 20–35.

[14] W. Song, Z. Ren, S. Y. Chen, Y. Meng, S. Biswas, P. Nandi, H. A. Elsen, P. X. Gao, S. L. Suib, *ACS Appl. Mater. Interfaces* **2016**, *8*, 20802–20813.

[15] X. Guo, X. Hu, D. Wu, C. Jing, W. Liu, Z. Ren, Q. Zhao, X. Jiang, C. Xu, Y. Zhang, N. Hu, *ACS Appl. Mater. Interfaces* **2019**, *11*, 21506–21514.

[16] Y. Liu, X. Xie, G. Zhu, Y. Mao, Y. Yu, S. Ju, X. Shen, H. Pang, *J. Mater. Chem. A* **2019**, *7*, 15851–15861.

[17] N. Kumar, M. Kumar, T. C. Nagaiah, V. Siruguri, S. Rayaprol, A. K. Yadav, S. N. Jha, D. Bhattacharyya, A. K. Paul, *ACS Appl. Mater. Interfaces* **2020**, *12*, 9190–9200.

[18] X. Deng, S. Öztürk, C. Weidenthaler, H. Tüysüz, *ACS Appl. Mater. Interfaces* **2017**, *9*, 21225–21233.

[19] V. Maruthapandian, M. Mathankumar, V. Saraswathy, B. Subramanian, S. Muralidharan, *ACS Appl. Mater. Interfaces* **2017**, *9*, 13132–13141.

[20] C. Tomon, A. Krittayavathananon, S. Sarawutanukul, S. Duangdangchote, N. Phattharasupakun, K. Homlamai, M. Sawangphruk, *Electrochim. Acta* **2021**, *367*, 137490.

[21] M. Shen, C. Ruan, Y. Chen, C. Jiang, K. Ai, L. Lu, *ACS Appl. Mater. Interfaces* **2015**, *7*, 1207–1218.

[22] C. Wan, Y. N. Regmi, B. M. Leonard, *Angew. Chemie* **2014**, *126*, 6525–6528.

[23] P. Wang, Y. Lin, L. Wan, B. Wang, *ACS Appl. Mater. Interfaces* **2019**, *11*, 37701–37707.

[24] X. Li, F. Dong, N. Xu, T. Zhang, K. Li, J. Qiao, *ACS Appl. Mater. Interfaces* **2018**, *10*, 15591–15601.

[25] J. A. Vigil, T. N. Lambert, J. Duay, C. J. Delker, T. E. Beechem, B. S. Swartzentruber, *ACS Appl. Mater. Interfaces* **2018**, *10*, 2040–2050.

[26] M. Yin, H. Miao, R. Hu, Z. Sun, H. Li, *J. Power Sources* **2021**, *494*, 229779.

[27] S. Bolar, S. Shit, P. Samanta, N. Chandra Murmu, T. Kuila, *Sustain. Energy Fuels* **2021**, *5*, 1148–1157.

[28] Y. Meng, W. Song, H. Huang, Z. Ren, S. Y. Chen, S. L. Suib, *J. Am. Chem. Soc.* **2014**, *136*, 11452–11464.

[29] K. Selvakumar, S. M. Senthil Kumar, R. Thangamuthu, K. Ganesan, P. Murugan, P. Rajput, S. N. Jha, D. Bhattacharyya, *J. Phys. Chem. C* **2015**, *119*, 6604–6618.

[30] K. Selvakumar, S. M. Senthil Kumar, R. Thangamuthu, G. Kruthika, P. Murugan, *Int. J. Hydrogen Energy* **2014**, *39*, 21024–21036.

[31] P. J. West, B. W. Byles, E. Pomerantseva, *Polyhedron* **2019**, *171*, 32–40.

[32] K. Selvakumar, S. M. S. Kumar, R. Thangamuthu, P. Rajput, D. Bhattacharyya, S. N. Jha,

ChemElectroChem **2018**, *5*, 3980–3990.

[33] F. Cheng, T. Zhang, Y. Zhang, J. Du, X. Han, J. Chen, *Angew. Chemie - Int. Ed.* **2013**, *52*, 2474–2477.

[34] J. M. Lee, S. B. Patil, B. Kang, S. Lee, M. G. Kim, S. J. Hwang, *J. Mater. Chem. A* **2018**, *6*, 12565–12573.

[35] Y. Han, Y. Yu, L. Zhang, L. Huang, J. Zhai, S. Dong, *Talanta* **2018**, *186*, 154–161.

[36] I. Roche, E. Chaînet, M. Chatenet, J. Vondrák, *J. Phys. Chem. C* **2007**, *111*, 1434–1443.

[37] E. Ríos, S. Abarca, P. Daccarett, H. Nguyen Cong, D. Martel, J. F. Marco, J. R. Gancedo, J. L. Gautier, *Int. J. Hydrogen Energy* **2008**, *33*, 4945–4954.

[38] T. N. Lambert, D. J. Davis, W. Lu, S. J. Limmer, P. G. Kotula, A. Thuli, M. Hungate, G. Ruan, Z. Jin, J. M. Tour, *Chem. Commun.* **2012**, *48*, 7931–7933.

[39] Y. Zhao, J. Zhang, W. Wu, X. Guo, P. Xiong, H. Liu, G. Wang, *Nano Energy* **2018**, *54*, 129–137.

[40] T. N. Lambert, J. A. Vigil, S. E. White, C. J. Delker, D. J. Davis, M. Kelly, M. T. Brumbach, M. A. Rodriguez, B. S. Swartzentruber, *J. Phys. Chem. C* **2017**, *121*, 2789–2797.

[41] K. Fujimoto, T. Okada, M. Nakayama, *J. Phys. Chem. C* **2018**, *122*, 8406–8413.

[42] D. Jampaiah, V. K. Velisoju, P. Venkataswamy, V. E. Coyle, A. Nafady, B. M. Reddy, S. K. Bhargava, *ACS Appl. Mater. Interfaces* **2017**, *9*, 32652–32666.

[43] X. Li, J. Liu, Y. Zhao, H. Zhang, F. Du, C. Lin, T. Zhao, Y. Sun, *ChemCatChem* **2015**, *7*, 1848–1856.

[44] D. Mondal, B. K. Paul, S. Das, D. Bhattacharya, D. Ghoshal, P. Nandy, K. Das, S. Das, *Langmuir* **2018**, *34*, 12702–12712.

[45] J. He, M. Wang, W. Wang, R. Miao, W. Zhong, S. Y. Chen, S. Poges, T. Jafari, W. Song, J. Liu, S. L. Suib, *ACS Appl. Mater. Interfaces* **2017**, *9*, 42676–42687.

[46] Y. Yang, X. Su, L. Zhang, P. Kerns, L. Achola, V. Hayes, R. Quardokus, S. L. Suib, J. He, *ChemCatChem* **2019**, *11*, 1689–1700.

[47] Y. Yamaguchi, R. Aono, E. Hayashi, K. Kamata, M. Hara, *ACS Appl. Mater. Interfaces* **2020**, *12*, 36004–36013.

[48] S. Kosasang, N. Ma, P. Wuamprakhon, N. Phattharasupakun, T. Maihom, J. Limtrakul, M. Sawangphruk, *Chem. Commun.* **2018**, *54*, 8575–8578.

[49] H. Huang, Y. Zhao, Y. Bai, F. Li, Y. Zhang, Y. Chen, *Adv. Sci.* **2020**, *7*, 2000012.

[50] Y. Jiao, L. Kang, J. Berry-Gair, K. McColl, J. Li, H. Dong, H. Jiang, R. Wang, F. Corà, D. J. L. Brett, G. He, I. P. Parkin, *J. Mater. Chem. A* **2020**, *8*, 22075–22082.

[51] Q. Wu, L. Jiang, L. Qi, E. Wang, G. Sun, *Int. J. Hydrogen Energy* **2014**, *39*, 3423–3432.

[52] C. Feng, M. B. Faheem, J. Fu, Y. Xiao, C. Li, Y. Li, *ACS Catal.* **2020**, *10*, 4019–4047.

[53] Y. Xie, Y. Yang, D. A. Muller, H. D. Abrunã, N. Dimitrov, J. Fang, *ACS Catal.* **2020**, *10*, 9967–9976.

[54] V. Duraisamy, R. Krishnan, S. M. Senthil Kumar, *ACS Appl. Nano Mater.* **2020**, *3*, 8875–8887.

[55] I. M. Mosa, S. Biswas, A. M. El-Sawy, V. Botu, C. Guild, W. Song, R. Ramprasad, J. F. Rusling, S. L. Suib, *J. Mater. Chem. A* **2015**, *4*, 620–631.

[56] D. J. Davis, T. N. Lambert, J. A. Vigil, M. A. Rodriguez, M. T. Brumbach, E. N. Coker, S. J. Limmer, *J. Phys. Chem. C* **2014**, *118*, 17342–17350.

[57] B. Yin, S. Zhang, H. Jiang, F. Qu, X. Wu, *J. Mater. Chem. A* **2015**, *3*, 5722–5729.

[58] C. Singh, A. Goyal, S. Singhal, *Nanoscale* **2014**, *6*, 7959–7970.

[59] R. Liu, J. Duay, S. B. Lee, *ACS Nano* **2010**, *4*, 4299–4307.

[60] Q. Liu, Z. Hu, L. Li, W. Li, C. Zou, H. Jin, S. Wang, S. L. Chou, *ACS Appl. Mater. Interfaces* **2021**, *13*, 16585–16593.

[61] Z. Ye, T. Li, G. Ma, Y. Dong, X. Zhou, *Adv. Funct. Mater.* **2017**, *27*, 1704083.

[62] M. Lübke, A. Sumboja, L. McCafferty, C. F. Armer, A. D. Handoko, Y. Du, K. McColl, F. Cora, D. Brett, Z. Liu, J. A. Darr, *ChemistrySelect* **2018**, *3*, 2613–2622.

[63] K. Li, J. Chen, Y. Peng, W. Lin, T. Yan, J. Li, *J. Mater. Chem. A* **2017**, *5*, 20911–20921.

[64] C. Belkessam, S. Bencherif, M. Mechouet, N. Idiri, J. Ghilane, *Chempluschem* **2020**, *85*, 1710–1718.

[65] L. Bigiani, A. Gasparotto, C. Maccato, C. Sada, J. Verbeeck, T. Andreu, J. R. Morante, D. Barreca, *ChemCatChem* **2020**, *12*, 5984–5992.

[66] B. Sidhureddy, S. Prins, J. Wen, A. R. Thiruppathi, M. Govindhan, A. Chen, *ACS Appl. Mater. Interfaces* **2019**, *11*, 18295–18304.

[67] Y. Hao, Y. Xu, J. Liu, X. Sun, *J. Mater. Chem. A* **2017**, *5*, 5594–5600.

[68] U. A. Paulus, T. J. Schmidt, H. A. Gasteiger, R. J. Behm, *J. Electroanal. Chem.* **2001**, *495*, 134–145.

[69] K. Selvakumar, V. Duraisamy, S. M. Senthil Kumar, *New J. Chem.* **2021**, *45*, 16913–16925.

[70] N. A. Anastasijević, V. Vesović, R. R. Adžić, *J. Electroanal. Chem. Interfacial Electrochem.* **1987**, *229*, 317–325.

[71] B. Kang, X. Jin, S. M. Oh, S. B. Patil, M. G. Kim, S. H. Kim, S.-J. Hwang, *Appl. Catal. B Environ.* **2018**, *236*, 107–116.

[72] J. M. Lee, S. J. Hwang, *J. Solid State Chem.* **2019**, *269*, 354–360.

10.1002/celc.202101303

Table of contents

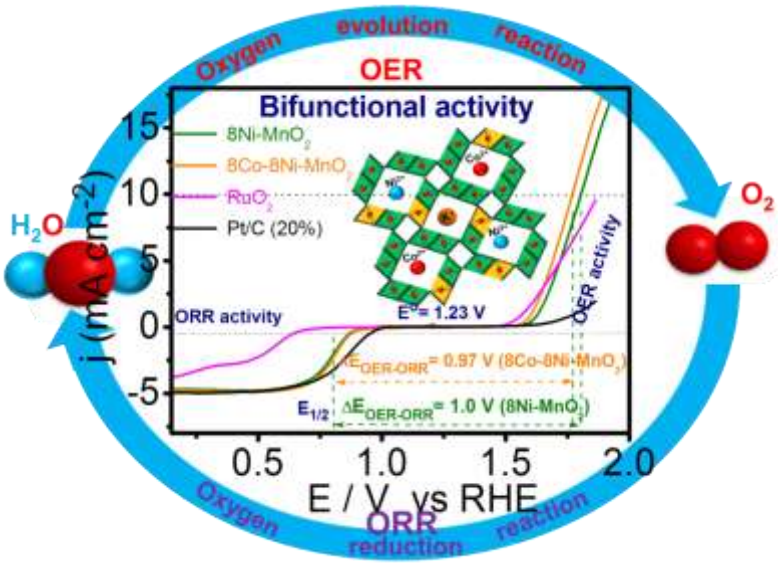

We developed various loading concentration of Ni^{2+} and Co^{2+} doped α-MnO_2 nanowire for tuning the Mn oxidation state and control the nanowire morphology. The simultaneous doping of both Co^{2+} and Ni^{2+} cations in α-MnO_2 leads to an enhanced synergistic effect without affecting crystallography and morphology. The 8Co-8Ni-MnO_2 catalyst demonstrates superior bifunctional OER/ORR activity owing to their high density of Mn^{3+} and Mn^{4+} sites.